RESEARCH ARTICLE

Open Access

Alignment & stability challenges for FCC-ee

Tessa K. Charles[1,2*] , Bernhard Holzer[3], Rogelio Tomas[3], Katsunobu Oide[3,4], Léon van Riesen-Haupt[5] and Frank Zimmermann[3]

*Correspondence:
tessa.charles@liverpool.ac.uk
[1] Department of Physics, University
of Liverpool, Liverpool, UK
[2] Cockcroft Institute, Warrington, UK
Full list of author information is
available at the end of the article

Abstract

In order to achieve its ultra-low vertical emittance (1 pm) and high luminosity (of up to 230×10^{34} cm^{-2} s^{-1} per collision point), the e$^+$e$^-$ Future Circular Collider (FCC-ee) requires a well-informed alignment strategy, powerful correction methods, and good understanding of the impact of vibrations. The large ring size, high natural chromaticity, small β^*, and the low coupling ratio make the FCC-ee design susceptible to misalignment and field errors, which if not properly addressed, threaten to increase the horizontal and vertical emittances and adversely affect the luminosity. Tight alignment tolerances around the 100 km ring would be a major cost driver and therefore alignment and stability need to be carefully studied. In this paper we present a status update, in which we apply analytical estimate methods, verified with simulation data, to determine the influence of the alignment of specific magnet types with the result informing the relative alignment tolerances. This is followed by simulations of a correction strategy that includes a large set of magnet misalignments and field errors. Finally, we also consider the tolerances on vibrations of quadrupoles through evaluating three cases: coherent vibration due to external seismic motion, vibrations resonant with the betatron frequency, and non-resonant, incoherent vibration.

1 FCC-ee lattice

The Future Circular e$^+$e$^-$ Collider (FCC-ee) is designed to operate at four beam energies—45.6, 80, 120, and 182.5 GeV—with luminosities varying from more than 10^{36} cm^{-2}s^{-1} at the lowest energy to about 10^{34} cm^{-2}s^{-1} at the highest [1]. In order to reach such a performance, a tight vertical focusing of the beam is required in the interaction regions along with smallest possible vertical beam emittance. Specifically, low vertical beta functions of 0.8–1.6 mm at the interaction point and vertical emittance values as small as 1–4 pm are foreseen.

The large bending radius of the FCC together with strong focusing will lead to a naturally small horizontal emittance, that would also provide the possibility to achieve the desired small vertical emittance of order 1 pm. However, with this low a target vertical emittance, smaller than in any previous e$^+$e$^-$ collider, the tolerance requirements for magnet field errors, beam-optics, and alignment accuracies need to be well understood. The FCC-ee has essentially the characteristics of a state–of–the–art light source as an ultra-low emittance storage ring, but includes the special features of a collider. Most notably, given the

Springer

relatively small design value of the vertical-to-horizontal emittance ratio of 2×10^{-3} in collision, a powerful correction algorithm is required to reduce the vertical dispersion and the betatron coupling introduced by magnet field errors, misalignments and roll angles. The vertical beam emittance without collision is strongly dominated by these imperfections, calling for a careful optimization. Similar to modern storage-ring light sources, damping rings and storage rings of future colliders, like the FCC-ee, require comprehensive simulations to ensure that their low design emittance values can be achieved through optics corrections and emittance tuning [2–4]. The optics tuning is equally challenging in future linear and hadron colliders [5–8] requiring large simulation campaigns to demonstrate their performance. In storage-ring colliders, the vertical emittance attainable with colliding beams will strongly depend on the vertical emittance of non-colliding beams and, in addition, on residual optics errors at the collision point. In this article, we study the vertical emittance without beam-beam effects.

In an ideal storage ring there is no vertical bending and therefore no vertical dispersion is introduced. Whilst alignment teams can achieve magnet-to-magnet alignments with impressive precision, and magnet designers achieve high field quality, even small misalignments and field errors can introduce vertical dispersion and coupling of motion between the horizontal and vertical planes.

As for all high-energy e^+e^- collider designs, in which the design value for the horizontal beam size at the collision point is determined by beam-beam effects including beamstrahlung, minimising the vertical emittance is desired in order to achieve a high luminosity. Consequently, we are seeking to understand the influence of various misalignments, field errors and vibrations, and devise strategies to counteract their effect. In this paper we present a status report of this ongoing endeavour, along with preliminary alignment tolerances.

There are a couple of sources of emittance growth in addition to coupling, residual vertical dispersion and β-beating introduced by magnet misalignments and field errors. Fringe fields of the compensating solenoid are predicted to increase the vertical emittance by 0.4 pm rad [9], and beam beam effects are also expected to increase the emittance [10, 11]. With these additional sources of emittance growth, it is especially important to minimise the emittance growth due to dispersion, coupling, and beta beating as much as possible.

The article is structured as follows. In Sect. 2, we describe analytical methods applied to estimate the expected contribution to the vertical emittance growth for different types of misalignments and magnets, through considering the average (or rms) changes in vertical dispersion and closed orbit caused by a given random distribution of errors. In Sect. 3 we then summarise the emittances achieved in MAD-X simulations for many random error seeds, after performing a series of correction techniques. In Sect. 4, we finally turn our attention to the impact of quadrupole vibrations through evaluating three cases: coherent vibration due to external seismic motion, vibrations resonant with the betatron frequency, and non-resonant, incoherent vibration. Finally we draw some conclusions.

However, before presenting the methods and results of our investigations, in the following subsection we start by introducing the misalignment types and related notations. The FCC-ee lattice used for our studies is the "version 301" lattice for $t\bar{t}$ operation with low-beta insertions at up to four interaction points (IPs), without the inclusion of compensating solenoids [12]. The main IP optics and beam parameters are summarized in

Table 1 Baseline beam parameters for the FCC-ee ttbar lattice with two Interaction Points [1]

Parameter	$t\bar{t}$
Beam energy [GeV]	182.5
Beam current [mA]	5.4
Number of bunches	33
Horizontal tune	394.252
Vertical tune	386.340
Natural relative hor. chromaticity, Q'_x/Q_x	−1.355
Natural relative vert. chromaticity Q'_y/Q_y	−5.397
Hor. chromaticity, Q'_x/Q_x	1.01×10^{-3}
Vert. chromaticity, Q'_y/Q_y	-2.13×10^{-3}
Hor. rms emittance ε_x [nm]	1.45
Vert. rms emittance ε_y [pm]	2.7
Hor. IP beta function β_x^* [m]	1
Vet. IP beta function β_y^* [mm]	1.6
$\mathcal{L}$ [10^{34} cm^{-2}s^{-1}]	1.5

Figure 1 Optics near the IP for the 182.5 GeV ttbar lattice. Top plot shows the beta functions in the IR, and the bottom plot shows the local chromaticity (ξ_{local}, Eq. (3)) and the horizontal dispersion (η_x)
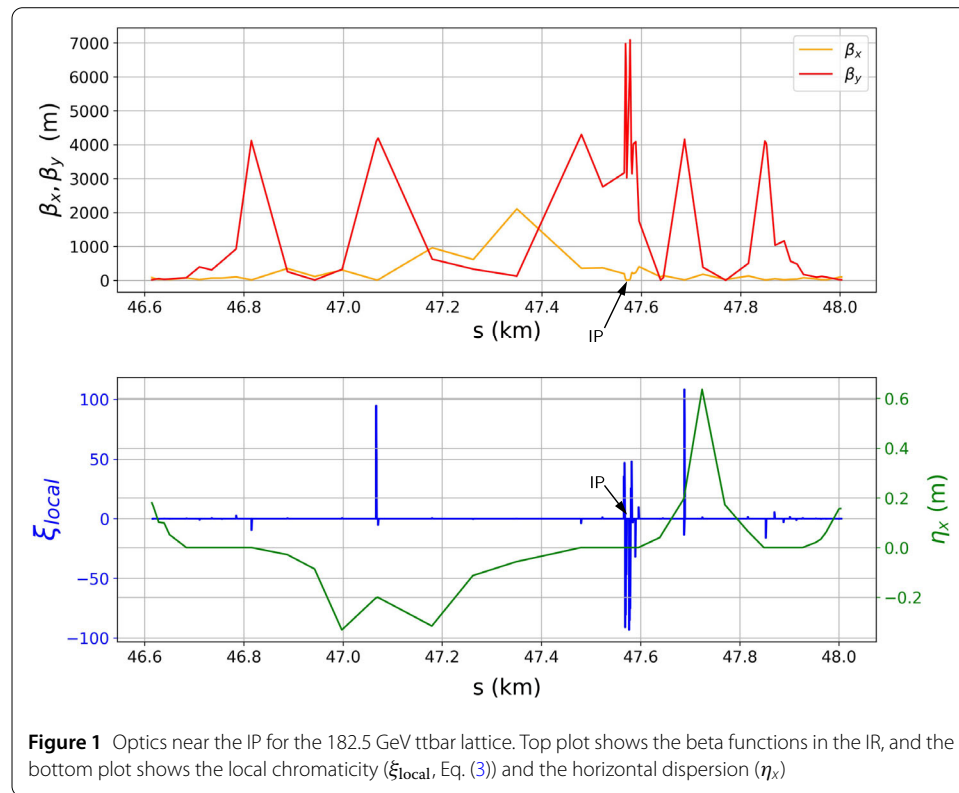
Table 1, assuming collisions in two of the interaction points. The design optical functions around the interaction region (IR) are shown in Fig. 1.

1.1 Misalignment definitions

In the following sections, magnets and girders are assigned misalignments in the horizontal (x), the vertical (y), and the longitudinal planes (s), as well as rotations around each of these axes (see Fig. 2). Straying from the convention used in the optics code MAD-X [13], the angles ΔPHI, ΔTHETA, and ΔPSI represent rotations about the x, y, and s axis, respectively, holding the centre of the magnet fixed. Increasing values indicate a clockwise rotation for ΔTHETA, and ΔPSI, but a counter-clockwise rotation for ΔPHI.

Figure 2 Definitions of misalignment errors
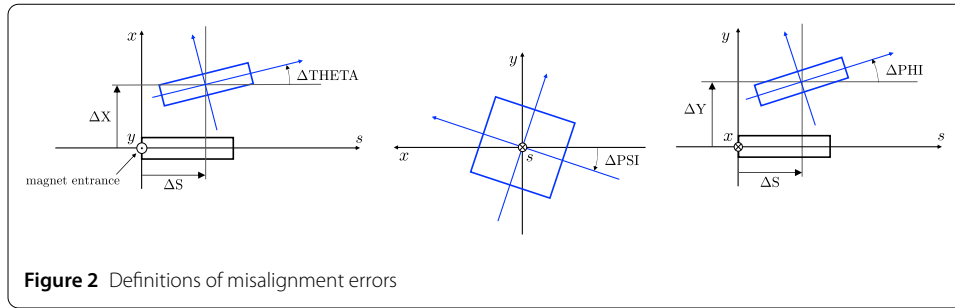
2 Analytical estimates

In this section we perform some analytical estimates of the emittance due to the misalignments of particular magnet types, in order to compare the relative contribution of various misalignment types to the overall allowed emittance budget, and the sensitivity for different magnets. Here, we follow the recipes and formulae of references [14, 15]. Evaluations of the analytical expressions can be compared to MAD-X simulations, in which errors are applied randomly via a 2.5 σ truncated Gaussian. Later, in Sect. 3, we present the results of a full emittance tuning simulation for various misalignments and field errors. In the present section we use a statistical approach to gauge the sensitivity of the machine to various types of errors.

2.1 Quadrupole roll errors

A quadrupole rotated about the z axis by an angle ΔPSI, will introduce a skew quadrupole field of strength $k_s = k_1 \sin(2\Delta\text{PSI}) \approx 2k_1 \Delta\text{PSI}$, which will introduce coupling between the vertical and horizontal motion.

The expected vertical emittance ϵ_y, introduced due to quadrupole roll errors randomly distributed via a Gaussian with a variance of $\langle\text{PSI}^2_{\text{quad}}\rangle$, is calculated as [14],

$$
\frac{\epsilon_y}{\langle\text{PSI}^2_{\text{quad}}\rangle} = \frac{J_z \sigma_\delta^2}{\sin^2(\pi Q_y)} \sum_{\text{quad}} \beta_y \eta_x^2 (k_1 L)^2 \\
+ \frac{J_x[1 - \cos(2\pi Q_x)\cos(2\pi Q_y)]\epsilon_x}{J_y[\cos(2\pi Q_x) - \cos(2\pi Q_y)]^2} \sum_{\text{quad}} \beta_x \beta_y (k_1 L)^2,
$$

(1)

where J_x, J_y and J_z denote the horizontal, vertical and longitudinal partition numbers respectively; Q_x and Q_y are the horizontal and vertical tunes; ϵ_x is the horizontal emittance, σ_δ is the normalised momentum spread at equilibrium, β_x, β_y and η_x are the horizontal and vertical beta functions and the horizontal dispersion at the position of the misaligned quadrupole with a normalised integrated strength of $k_1 L$.

The first term in Eq. (1) is the emittance increase due to vertical dispersion that comes from coupling to horizontal dispersion in the misaligned quadrupoles. The second term captures the coupling between the horizontal and vertical transverse motion and the extent to which effects that would only generate horizontal emittance in an uncoupled machine, produce vertical emittance.

Figure 3 shows Eq. (1) applied to arc quadrupoles, IR quadrupoles, and finally all quadrupoles, over roll angles ranging from an rms value of 10 μrad through to 50 μrad in steps of 5 μrad. Included in Fig. 3 are MAD-X simulation results. 100 random seeds were
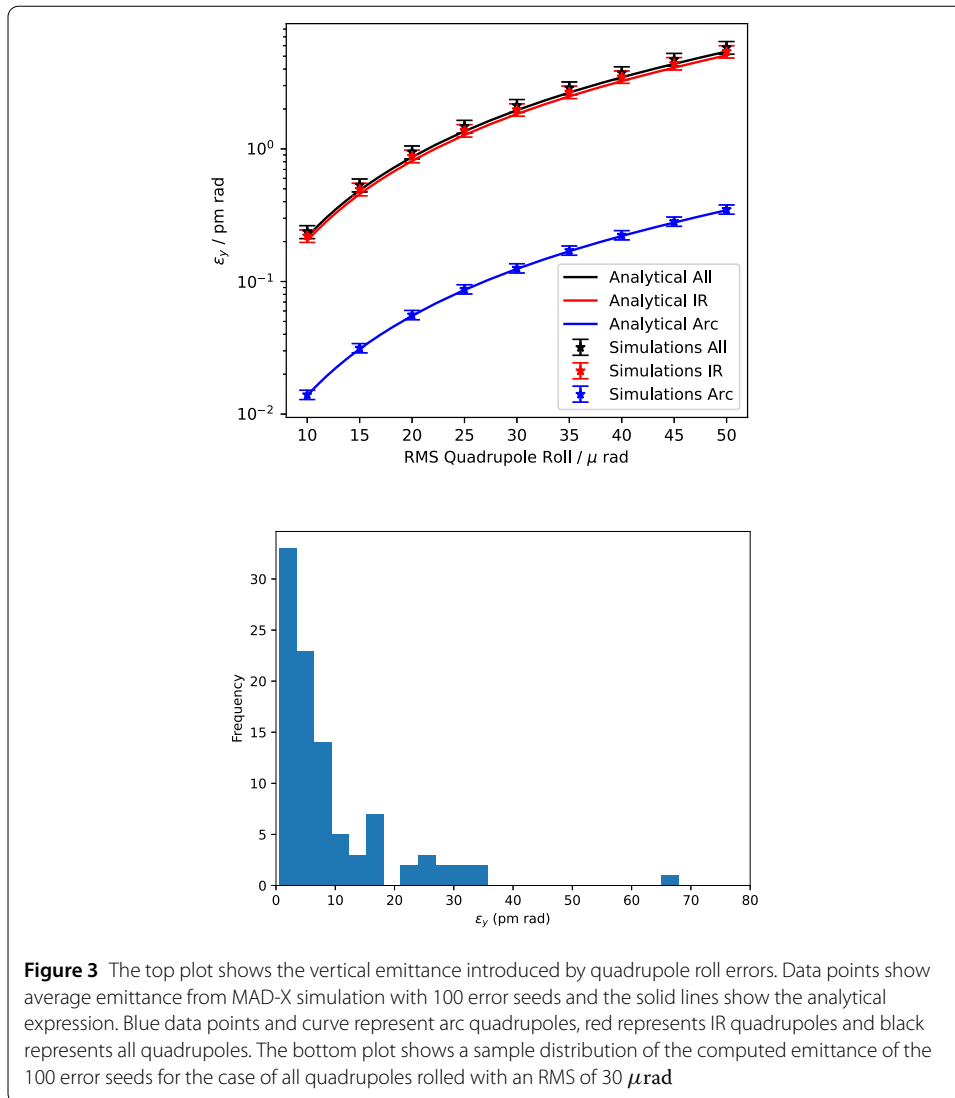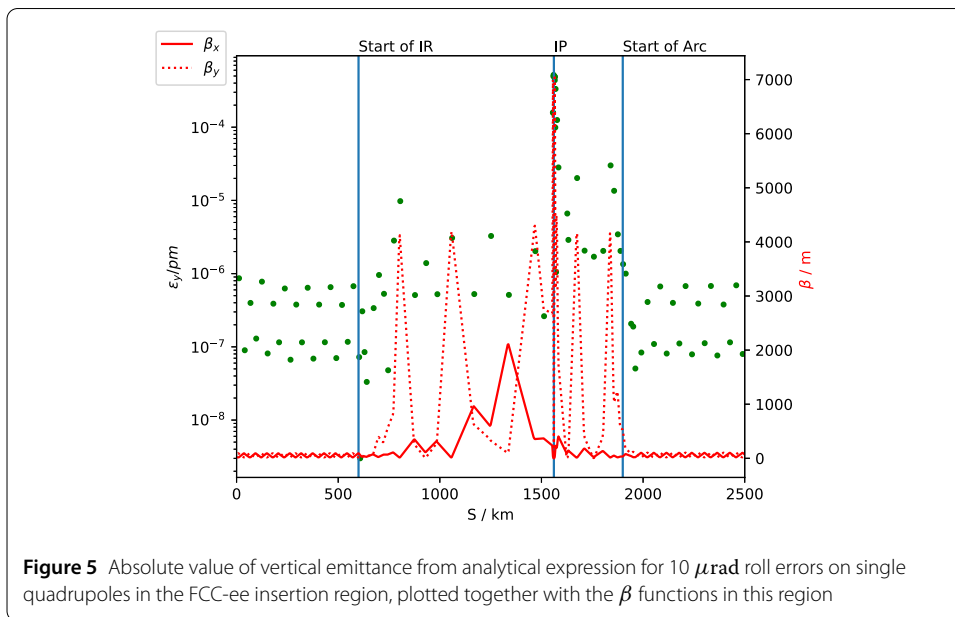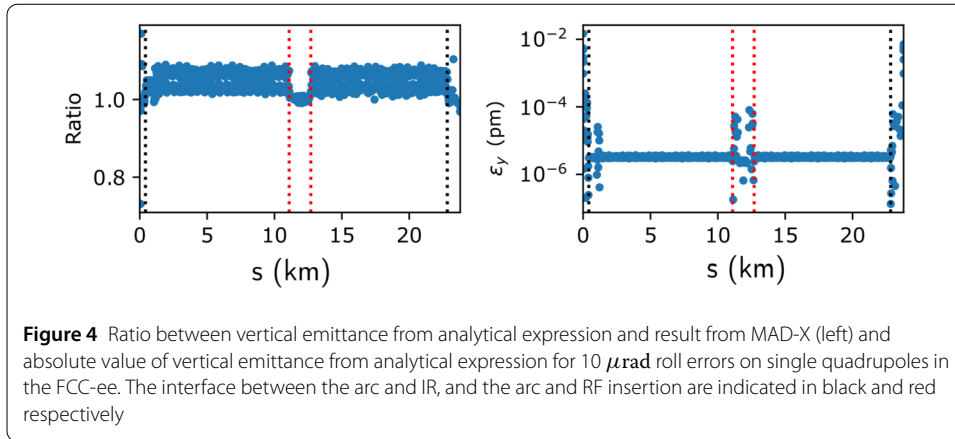
Figure 3 The top plot shows the vertical emittance introduced by quadrupole roll errors. Data points show average emittance from MAD-X simulation with 100 error seeds and the solid lines show the analytical expression. Blue data points and curve represent arc quadrupoles, red represents IR quadrupoles and black represents all quadrupoles. The bottom plot shows a sample distribution of the computed emittance of the 100 error seeds for the case of all quadrupoles rolled with an RMS of 30 μrad

used for each quadrupole roll angle, with the data points showing the average emittance of the 100 seeds. To illustrate a typical distribution, Fig. 3 also shows the emittance distribution for the 100 seeds used in the simulation of all quadrupoles rolled with an RMS of 30 μrad.

Figure 3 demonstrates not only that the analytical expression well predicts the vertical emittance growth, but also that the quadrupoles in the IR have a far greater influence on the emittance than arc quadrupoles, with the contribution of the arc quadrupoles being about 10 % of the total vertical emittance growth.

A closer look at the influence of individual quadrupoles is taken in Fig. 4, where one-by-one, going from one IP to the next, each quadrupole is rotated by 10 μrad whilst leaving all other quadrupoles perfectly aligned. The left plot in Fig. 4 shows the ratio between the Eq. (1) prediction for the vertical emittance and the MAD-X calculation of the vertical emittance. The analytical expression predicts the emittance to within $\pm 10\%$ for the majority of the quadrupoles, with a few exceptions noted near the IPs.

Figure 4 Ratio between vertical emittance from analytical expression and result from MAD-X (left) and absolute value of vertical emittance from analytical expression for 10 μrad roll errors on single quadrupoles in the FCC-ee. The interface between the arc and IR, and the arc and RF insertion are indicated in black and red respectively

Figure 5 Absolute value of vertical emittance from analytical expression for 10 μrad roll errors on single quadrupoles in the FCC-ee insertion region, plotted together with the β functions in this region
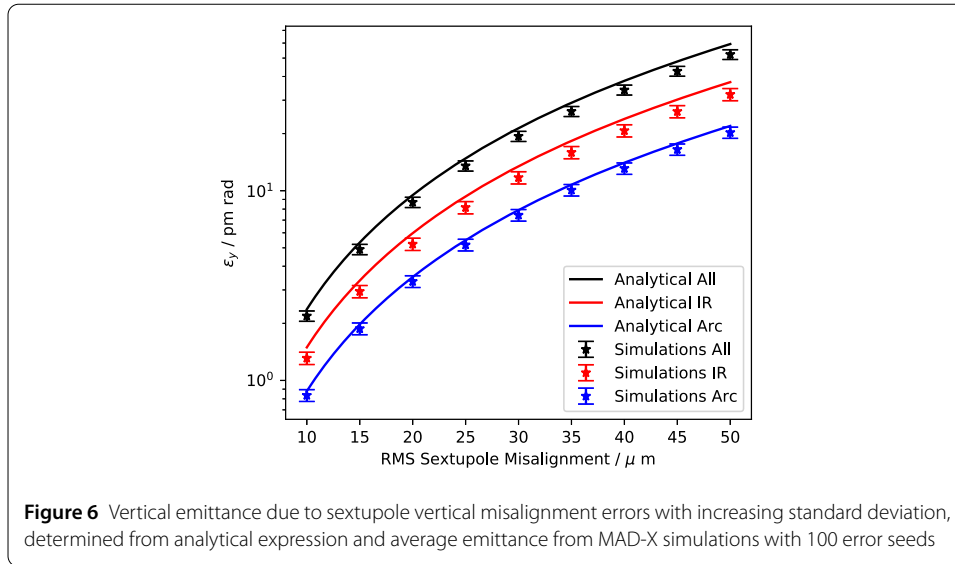
The right picture of Fig. 4 presents the vertical emittance introduced by the rotation of individual quadrupoles. This plot highlights that for roll errors of similar magnitude, a small group of quadrupoles located in the IR can introduce a vertical emittance increase of several orders of magnitude greater than all other quadrupoles. This is due to the large beta function in these sections. Figure 4 allows us to pin-point which magnets are most susceptible to increasing the vertical emittance through an uncorrected roll angle.

By looking at Eq. (1), we can see that apart from the quadrupole strength, one of the drivers for a large impact on emittance is the optics at the location of the rolled quadrupole. This is one of the key reasons why the emittance contribution from the insertion region is larger than that from the arcs. To visualise this we can zoom into the interaction region and plot the optics as well as the contribution to the emittance growth from a 10 μrad roll. This is shown in Fig. 5.

2.2 Sextupole misalignments

Similar to a rolled quadrupole producing a skew quadrupole field, a vertically offset sextupole will also produce a skew quadrupole field with a strength $k_s = k_2 \Delta Y$, where k_2 is

Figure 6 Vertical emittance due to sextupole vertical misalignment errors with increasing standard deviation, determined from analytical expression and average emittance from MAD-X simulations with 100 error seeds

the normalised sextupole strength. Therefore Eq. (1) can be easily adapted for sextupole misalignments by replacing k_1 with $k_2/2$ and $\langle \text{PSI}^2_{\text{quad}} \rangle$ with the standard deviation of the vertical sextupole misalignment, $\langle \text{Y}^2_{\text{sext}} \rangle$ [16].

In a similar manner to before, the sextupoles were randomly misaligned in the vertical plane in MAD-X simulations using 100 random seeds and the calculated vertical emittance was compared to the analytical expression for the expected vertical emittance. Figure 6 displays the result. The results are shown for the arc sextupoles, the strong IR sextupoles used for local chromaticity correction, and all of the sextupoles together. Similar to what was observed for the case of the roll quadrupoles, the contribution from the relatively few IR sextupoles is noticeably larger than that of the arc magnets due to the fact that these magnets are stronger and the β functions are significantly larger in this area, although the difference is not as pronounced as in the case of the rolled quadrupoles.

When misaligning individual sextupoles by 10 μm, one at a time, as illustrated in Fig. 7, we can examine how well the analytical equation predicts the emittance due to individual sextupoles, and also compare how big the impact of individual sextupoles is. The left plot in Fig. 7, shows that there is an even better agreement between the formulas and simulations than for the case of quadrupoles. From the right plot in Fig. 7, we again infer that a small number of sextupoles in the IR are capable of increasing the vertical emittance by two orders of magnitude more than the majority of sextupoles. Unlike the case of the rolled quadrupoles, there is a larger spread of the sensitivities inside the arcs. The qualitative difference in sensitivity between the quadrupole roll and sextupole misalignments can be attributed to the relative difference in strengths between the arc magnets and IR magnets for these two magnet types.

The arc quadrupoles—all of about the same strength—are much weaker than the final-focus quadrupoles, while strong arc sextupoles come relatively closer to the strength of the few sextupoles situated in the final focus. The strength of each sextupole pairs located in the arcs, is individually powered and optimised for maximum dynamic aperture. As a result, there is a spread in arc sextupole strengths, leading to the spread in sensitivity seen in Fig. 7.
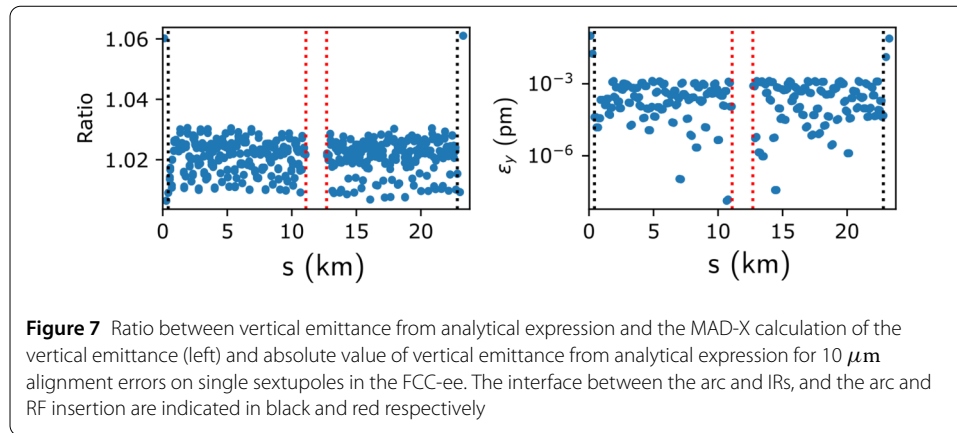
Figure 7 Ratio between vertical emittance from analytical expression and the MAD-X calculation of the vertical emittance (left) and absolute value of vertical emittance from analytical expression for 10 μm alignment errors on single sextupoles in the FCC-ee. The interface between the arc and IRs, and the arc and RF insertion are indicated in black and red respectively

Table 2 rms misalignment values used in simulations presented in this paper. The definition of the misalignment parameters are defined in Fig. 2. Note that values are not tolerance specifications, as there is an ongoing iterative process to determine the alignment level achievable and the acceptable machine performance

Type	ΔX (μm)	ΔY (μm)	ΔPSI (μrad)	ΔS (μm)	ΔTHETA (μrad)	ΔPHI(μrad)
Arc quadrupoles*	50	50	300	150	70	70
Arc sextupoles*	50	50	300	150	70	70
Dipoles	1000	1000	300	1000	0	0
Girders	150	150	–	1000		
IR quadrupole	100	100	250	250	70	70
IR sextupoles	100	100	250	250	70	70

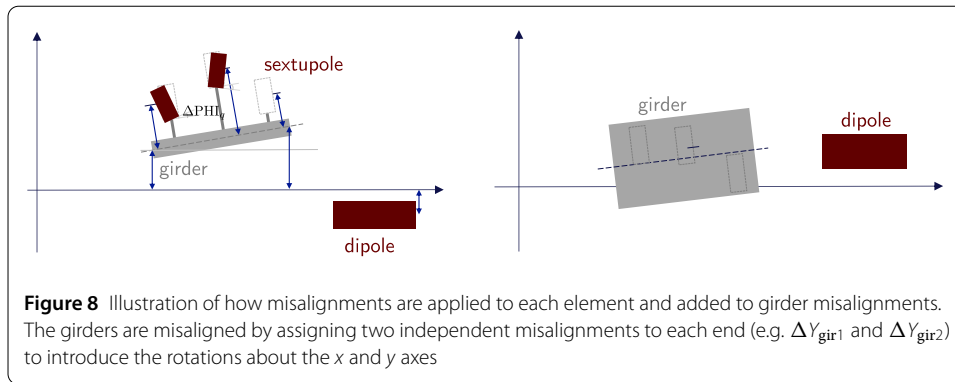* misalignments relative to girder placement

Table 3 rms gradient errors used in all simulations presented in this paper. Note that values are not tolerance specifications, as there is an ongoing iterative process to determine the field precision achievable and the acceptable machine performance

Type	Field Errors
Arc quadrupole	$\Delta k/k = 2 \times 10^{-4}$
Arc sextupoles	$\Delta k/k = 2 \times 10^{-4}$
Dipoles	$\Delta B/B = 1 \times 10^{-4}$
IR quadrupole	$\Delta k/k = 1 \times 10^{-4}$
IR sextupoles	$\Delta k/k = 2 \times 10^{-4}$

3 Emittance tuning simulations

A series of correction techniques have been applied in MAD-X and Python. A complete description of the correction strategy is planned for an future full-length paper. In this section we outline the main correction steps undertaken and summarise the main results for a collection of misalignments and field errors. All errors were assigned randomly via a Gaussian distribution truncated at 2.5 sigma, for 100 random seeds. Tables 2 and 3 show the rms values of the misalignments and field errors applied. Please note BPM misalignments are not yet included and this is currently being investigated.

To assign the misalignments (according to the rms values in Tables 2 and following the definitions in Fig. 2), each magnet was misaligned in *x*, *y*, and *s*, and then the rotations applied about the center of the magnet. Girders are used in the arcs, in between dipoles, carrying a quadrupole and two sextupoles and have an average length of 3.9 m. To in-

Figure 8 Illustration of how misalignments are applied to each element and added to girder misalignments. The girders are misaligned by assigning two independent misalignments to each end (e.g. ΔY_{gir1} and ΔY_{gir2}) to introduce the rotations about the *x* and *y* axes

troduce the girder misalignments two independent misalignments in both *x* and *y* were assigned to each end of the girder and the girder itself assumed rigid. As a result, the misalignments in *x* and *y* at each end of the girder are specified, rather than rotation angles, ΔTHETA and ΔPHI. The misalignments of the magnets on the girder are then added to the misalignment of the girder at the position along the girder where the magnet is located. Figure 8 illustrates the accumulation of multiple misalignments. Note that values presented in Tables 2 and 3 are the values used in the simulations being presented. They are not tolerance specifications, as there is an ongoing iterative process to determine the alignment level achievable and the acceptable machine performance.

3.1 Correction algorithm

The correction strategy is based on macros written in Python. See references [17, 18] for detail of the various correction techniques. The corrections were performed using 3276 dipole corrector magnets and 3276 single-plane BPMs (one installed at every quadrupole), 1264 skew quadrupoles and 1264 trim quadrupoles (installed at every sextupole). Several steps were performed and optimised, those steps are as follows:

(1). Mono-energetic beam: Initially the beam energy was set to a virtual value of 1 GeV where synchrotron light effects can be neglected. The RF voltage set to zero, and energy loss from synchrotron radiation was not included in the simulations. The 1 GeV beam without synchrotron radiation is considered a valid representation of a full-energy fully tapered machine. Note, by 'tapering', we refer to the gradual reduction in magnet field strength around the ring, between RF sections, to account for the reduced beam energy due to synchrotron radiation [1, 19]. At the final stage of the correction strategy (see below), synchrotron radiation is turned on for the emittance calculation, which is based upon the Chao formalism for equilibrium emittance [20].

(2). Starting with a linear machine: The next step of this strategy was to set all of the sextupole strengths to zero, to avoid strong non-linear effects from the sextupole fields. In a loop throughout the correction strategy, the sextupole strengths were increased by steps of 10% at a time. Once at 100% of the sextupole design value, additional coupling and vertical dispersion correction ensure that low vertical emittance can be achieved.

(3). For each value of the sextupole strength, the gradient errors and misalignment tolerances were introduced in separate steps. Firstly, the quadrupole normalised gradient errors were introduced to all quadrupoles following a random Gaussian distribution with a standard deviation of $\sigma = 1 \times 10^{-4}$. Then this was immediately followed by a weighted β-beat correction whereby all BPMs within 690 meters of the IP were given a weighting

factor of 10, while a weighting factor of 1 was applied to every other BPM. The gradient errors of the arc quadrupoles and all sextupoles were then increased to $\sigma = 2 \times 10^{-4}$. The random seed chosen for these two error assignments was the same, to ensure that the gradient errors were not re-distributed, but increased in magnitude when this second error step was applied. Following additional weighted β-beating correction, field errors were applied to the sextupoles and dipoles with standard deviations of $\sigma = 2 \times 10^{-4}$ and $\sigma = 1 \times 10^{-4}$, respectively. At this stage, finally, all misalignment errors were introduced and the correction scheme could continue.

In more detail the correction strategy went through the following logic:

1. Sextupoles strengths were set to zero.
2. Gradient errors applied
   (a) Quadrupole field errors introduced at half of the target field error value.
   (b) Weighted β-beat correction was performed and tune re-matched.
   (c) Quadrupole field errors increased to target field error value.
   (d) Weighted β-beat correction was performed and tune re-matched.
   (e) Sextupole and dipole field errors introduced.
   (f) Weighted β-beat correction was performed and tune re-matched.
3. Misalignments applied to all magnets and girders.
4. Tune re-matched to the nominal tune, and SVD orbit correction performed.
5. β-beat correction (which includes horizontal dispersion correction) applied, and if needed SVD orbit corrected and tune rematched.
6. Coupling correction, followed by β-beat correction (including horizontal dispersion correction) and combined coupling and vertical dispersion correction.
7. Sextupole field errors introduced and sextupoles set to 10% of their design strength.
   (a) Coupling correction, combined coupling and dispersion correction and β-beating and horizontal dispersion correction applied.
   (b) Sextupole strengths increased by 10% and Step 7 repeated until the design sextupole strength is reached.
   (c) Throughout correction, the tune is re-matched and additional orbit correction applied when necessary.
8. Once at 100% of the design sextupole strength, additional coupling, dispersion and β-beating and horizontal dispersion correction, and chromaticity correction are applied (more details provided below).

Due to the strong influence of the non-linear fields on the beam optics, Step 7 makes up the bulk of the computation. Throughout this step a possible vertical orbit fluctuation will lead to an increasing source of coupling, that exacerbates any further correction scheme. To mitigate this unavoidable effect, we iterate for each increase in sextupole strength through a careful coupling correction, a combined coupling and dispersion correction, and β-beat correction which includes horizontal dispersion correction. During each step of the iteration, the orbit and tune were monitored and if the rms orbit became too large an orbit correction was applied to keep feed down effects from the strong sextupole fields limited. In very much the same way, an additional tune re-match was introduced, in case the tune shifted to far away from its nominal value.

In the final step, after a successful correction of coupling, dispersion and β-beating to a suitable level, additional corrections were applied to balance the vertical emittance and β-beating. At this fine-scale level of correction, we face the issue of a trade-off between β-

beat correction and the simultaneous coupling and dispersion correction. A decision can be made in the correction algorithms as to whether more importance is given to β-beating or the vertical emittance. The final values of both, the β-beating and vertical emittance, will be small, but in order to push one of the two to even lower values, the other inevitably increases slightly. This is due to the small residual orbit distortion and accordingly to the fact that beam optics (i.e. beta function), orbit fluctuations (betatron oscillations), dispersion and finally coupling cannot be considered as independent parameters anymore. When the orbit passes slightly off-centre through the trim quadrupoles, and their strength changes in the context of the β-beat correction, a small vertical kick is introduced due to the feed down effect in these quadrupole lenses. Again, to reiterate, this effect is small and is most visible once the orbit, dispersion, coupling and β-beat have already reached a high level of correction.

Chromaticity correction is applied through the arc sextupoles, leaving the local chromaticity correction sextupoles in the IR untouched. Despite the sextupole strength needing to vary by only a small amount (by on average 1.9%) this was enough to increase the vertical emittance and make the coupling and dispersion correction less effective. Therefore, at this stage in the correction strategy the coupling-dispersion response matrix is re-measured, and then additional coupling-dispersion correction applied.
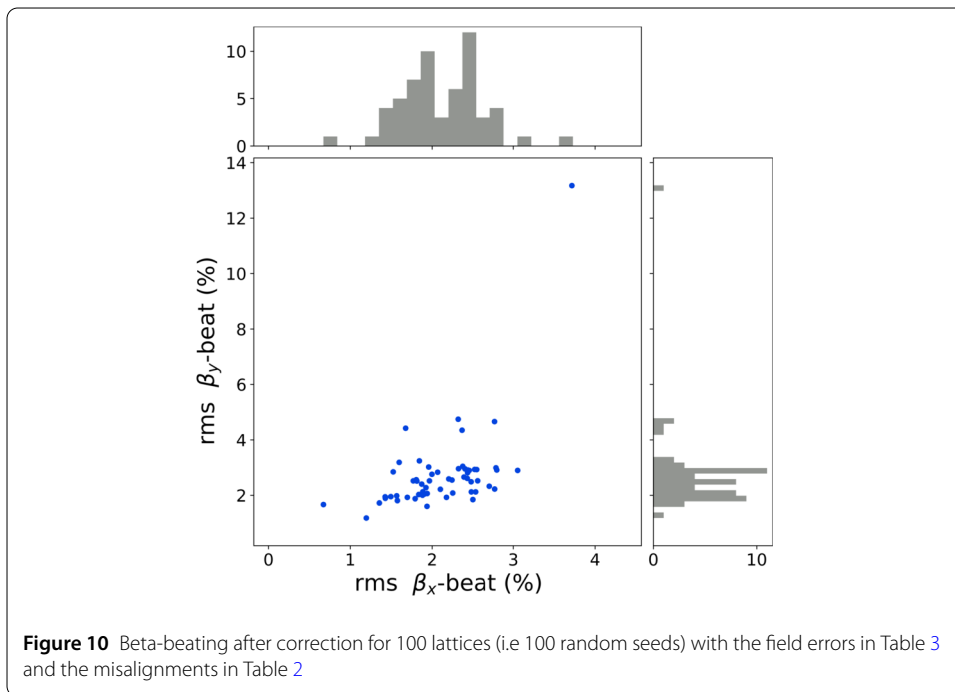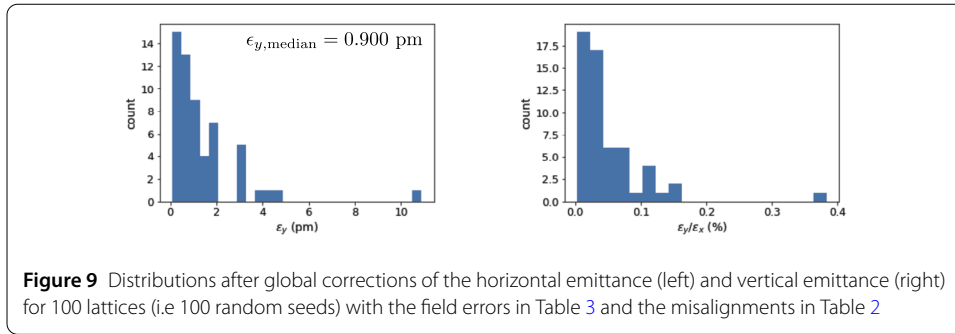
At this final correction stage, an acceptable limit can be placed on either the vertical emittance or the rms β-beating. For the results presented in this report, the acceptable limit for vertical rms β-beating was placed at 3% (note many of the seeds will still achieve an rms beat beating of less than 3%).

Based on the experience made during these simulations, another special feature has been introduced to gain best correction efficiency: In step 8 of the above listed correction scheme, the singular value cut-off level is incrementally lowered to include more singular values until the required β-beating limit was achieved. By stepping through various SVD cut off values, we can ensure that the pseudo-inverse calculation takes enough details into account to reach the desired level of correction. Still, caution is advised: Lowering the cut-off level of the SVD values too much will include too much detail and the pseudo-inverse calculation starts incorporating artificial noise. This stepping through SVD cut-off values is done twice, once for β-beat correction and once for the correction of coupling and dispersion. Then a final check will reveal if the β-beating and vertical emittance are sufficient.

3.2 Simulations results

The correction algorithm was applied to 100 different random error distributions. For these results presented, no BPM errors were included. Figure 9 shows the distributions of the vertical and horizontal emittances of the 100 random seeds after correction. The left most plot in Fig. 9 shows 84% of the seeds achieve a vertical emittance of less than 2.3 pm, with the distribution showing a median emittance of 0.90 pm. Note that these emittance values are resulting from the misalignments and field errors after corrections and does not include the emittance growth expected from solenoid fringe fields, or the effect of BPM errors.

The β-beating after correction for the same 100 seeds can be seen in Fig. 10, with almost all seeds resulting in a final rms vertical β-beating of less than 5%.

Figure 9 Distributions after global corrections of the horizontal emittance (left) and vertical emittance (right) for 100 lattices (i.e 100 random seeds) with the field errors in Table 3 and the misalignments in Table 2

Figure 10 Beta-beating after correction for 100 lattices (i.e 100 random seeds) with the field errors in Table 3 and the misalignments in Table 2

3.3 Discussion of emittance tuning

3.3.1 Orbit

The projected vertical emittance due to dispersion varies noticeably when the orbit is corrected. The contribution to projected vertical dispersion from the corrected orbit is given by [14],

$$
\overline{\left(\frac{\langle\eta_y^2\rangle}{\beta_y}\right)} \approx \frac{1}{16\sin^2(\pi Q_y)}\overline{\left(\frac{\langle y_c^2\rangle}{\beta_y}\right)}\sum_{n_c}^{N_{\mathrm{corr}}}\left[\left|\int_{n_c}^{n_c+1}(K_2\eta_x - K_1)\beta_y\,dz\right|^2\right.
$$
$$
\left. + \left|\int_{n_c}^{n_c+1}(K_2\eta_x - K_1)\beta_y e^{i2\psi}\,dz\right|^2\right],
$$

(2)

where Q_y denotes the vertical tune, y_c the closed orbit, n_c the position of a correction (and $n_c + 1$ denotes the position of the next corrector), N_{corr} the total number of correctors, and ψ the vertical phase advance. Finally, K_1 and K_2 are the normalised quadrupole and sextupole field gradients, and l_q and l_s are the lengths of the quadrupoles and sextupole magnets respectively.

Equation (2) is dependent upon the local chromaticity,

$$\xi_{\text{local}} = (K_2 l_s \eta_x - K_1 l_q)\beta_y \tag{3}$$

and local off-energy stopband,

$$\Delta_{\text{local}} \propto (K_2 l_s \eta_x - K_1 l_q)\beta_y e^{i2\psi}. \tag{4}$$

These local values are often much larger in magnitude than the average values in the FCC-ee IR. Whilst the local chromaticity is usually positive in the dispersion regions to counteract the negative chromaticity of the dispersion-free regions, in the FCC-ee IR the local chromaticity swings between extremes of positive and negative values (Fig. 1). Despite this, the dispersion from the corrected orbit is usually smaller than for the uncorrected orbit (thanks to the $\frac{\langle y_c^2 \rangle}{\beta_y}$ term becoming smaller). Unlike the uncorrected orbit counterpart equation to Eq. (2) which is not included here, the magnitude of the ξ_{local} and Δ_{local} are important, with no opportunity for negative and positive values to cancel out.

Within the FCC-ee IR, the sextupole positioning and strength is optimised for local chromaticity correction as well as crab optics in what is referred to as a virtual crab-waist scheme [21]. Therefore the vertical dispersion due to the closed orbit distortion cannot be reduced by reducing the local chromaticity, and attention should be placed on ensuring the orbit is well corrected where ξ_{local} and Δ_{local} are large. Attention must also be given to ensure any changes in the sextupole strengths do not affect the non-linear chromaticity correction and in turn the momentum acceptance.
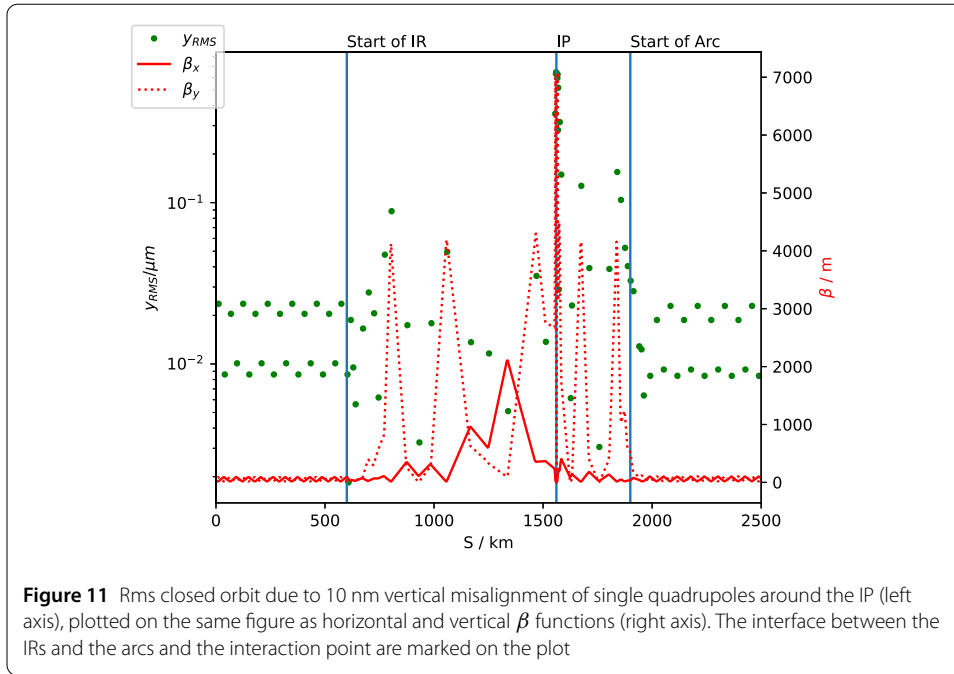
Another aspect to consider is the fact that the impact of magnet misalignments on the closed orbit depends on the strength of the misaligned magnet and the β function within that magnet. To understand how the sensitivity of the closed orbit depends on the vertical misalignment of different quadrupoles, a study was performed in which individual quadrupoles were misaligned vertically by 10 nm and the rms closed orbit was recorded, the results are shown in Fig. 11. Figure 11 shows that misalignment of some IR quadrupoles causes the rms closed orbit to be an order of magnitude larger than from misalignments on arc quadrupoles. This is especially the case when the vertical β function, also plotted in Fig. 11, in the magnets is especially large. This indicates that these magnets should have tighter alignment tolerances than other magnets.

Finally, one of the subjects for a future study is the case with diffusive motion of the ground such as described by the ATL-law [22, 23].

4 Tolerances for quadrupole vibration

The vertical displacement of a beam caused by a quadrupole vibrating with an amplitude Δy_q and an angular frequency ω_q at the vertical phase advance ϕ_q from the IP is given as an infinitesimal sum over the contribution from the $-n$th tune:

$$
\begin{aligned}
\Delta y^* &= \sum_n \sqrt{\beta^* \beta_q} \exp(-n T_0/\tau_y + i\omega_q n T_0) \sin(\phi_q + n\mu_y) k_q \Delta y_q \\
&= \sum_n \sqrt{\beta^* \beta_q} \exp(-n\alpha_y + in\mu_q) \sin(\phi_q + n\mu_y) k_q \Delta y_q,
\end{aligned}
\tag{5}
$$

Figure 11 Rms closed orbit due to 10 nm vertical misalignment of single quadrupoles around the IP (left axis), plotted on the same figure as horizontal and vertical β functions (right axis). The interface between the IRs and the arcs and the interaction point are marked on the plot

where μ_y, T_0 and τ_y, are the vertical betatron angular tune, the revolution and damping times respectively, $k_q \equiv K_1 l_q$, $\alpha_y \equiv T_0/\tau_y$, $\mu_q \equiv \omega_q T_0$, and β^*, β_q, k_q are the beta functions at the IP, the quadrupole, and the focusing strength of the quadrupole respectively. The vibration amplitude Δy_q can be random at each quad, or coherent due to external seismic motion.

In this section let us examine three types of vibrations: (i) group resonance to a seismic plane wave, (ii) temporal resonance of each quadrupole, (iii) non-resonant vibration of each quadrupole. We assume that each quadrupole simply follows the ground motion, and no amplification nor reduction by the supporting structure is taken into account.

4.1 Vibration due to seismic motion

First let us evaluate the coherent part by assuming that the quadrupoles are distributed over the ring uniformly with the betatron phase $\phi_q = m\Delta\phi_q$, and also physically located over a ring of the radius R with a constant separation azimuthal angle θ_q, *i.e.*,

$$X_m + iY_m = R\exp(im\theta_q), \tag{6}$$

where m is an integer from 1 through to N_q, the number of quadrupoles around the ring (see Fig. 12).

Then if the quadrupoles follow the surface seismic wave on the ground, the displacement Δy_m of the m-th quadrupole is written as

$$\Delta y_m = u\exp\big(i(k_X X_m + k_Y Y_m - \omega_q t)\big), \tag{7}$$

where $k_{X,Y}$ are the components of the seismic wave number vector, and u represents the amplitude. Here we just set $k_X = k$ and $k_Y = 0$ for simplicity without losing generality if the ring is approximated by a circle. So we may sum up the term $\sin(\phi_q + n\mu_y)\Delta y_q$ in Eq. (5)

Figure 12 A uniform distribution of quadrupoles over a perfect circle is assumed
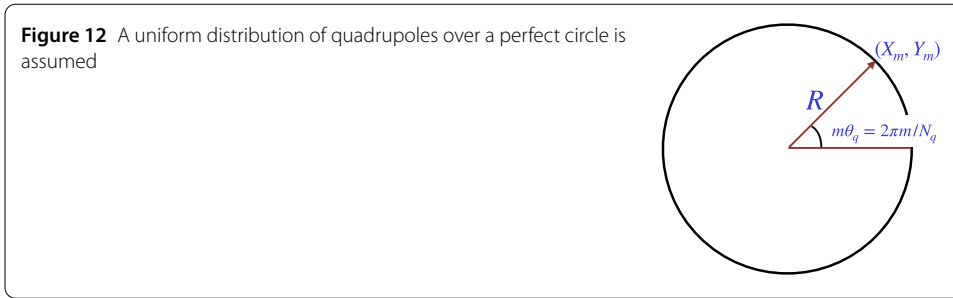
over quadrupoles as

$$
\begin{aligned}
N_q d_s &= \sum_{m}^{N_q} \sin(\phi_q + n\mu_y)\Delta y_m \\
&= \sum_{m}^{N_q} \sin(m\Delta\phi_q + n\mu_y) u \exp\big(i(kR\cos m\theta_q - \omega_q t)\big) \\
&= u \sum_{\ell=-\infty}^{\infty} \sum_{m}^{N_q} \sin(m\Delta\phi_q + n\mu_y) J_\ell(kR) i^\ell \exp(i\ell m\theta_q - i\omega_q t),
\end{aligned}
\tag{8}
$$

where we have applied $\exp(ix\cos z) = \sum_\ell i^\ell J_\ell(x)\exp i\ell z$. Although there may be a resonance in Eq. (8) at $\ell \sim \pm\Delta\phi_q/\theta_q$, the index ℓ becomes very large in the case of the FCC-ee Z lattice, where $\Delta\phi_q = 83.5$ deg, $\theta_q = 360/924 \sim 0.390$ deg, and $\ell \sim 214$. As for N_q, we have taken only vertical focusing quadrupoles (QDs) into account. Thus the coefficient J_ℓ becomes infinitesimal for such a large ℓ, so the resonant effect is negligible. The expression Eq. (8) is similar to Ref. [24], but the suppression by the large ℓ is basically due to the large number of quadrupoles in the ring.

We may look at the term $\ell = 0$ in Eq. (8), which is written as

$$
d_{s0} = u J_0(kR) \frac{\sin(\mu_y/2)\sin(n\mu_y + (\mu_y - \Delta\phi_q)/2)}{\sin(\Delta\phi_q/2)}.
\tag{9}
$$

We know $J_0(x) \leq 1$, and the rest of the rhs of Eq. (9) is close to unity. Then the magnitude of the coherent component is smaller than the random component:
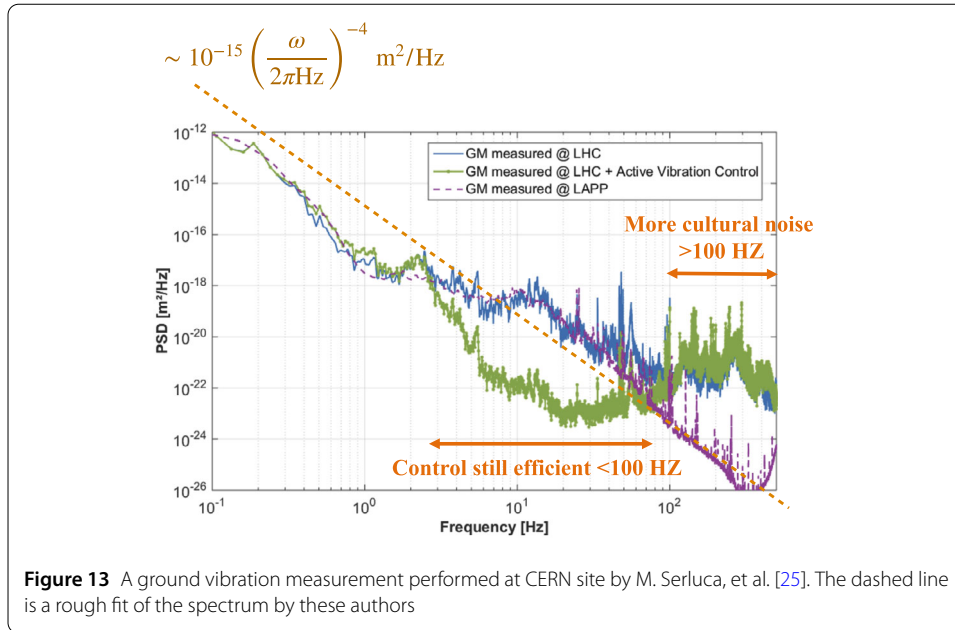
$$
|d_{s0}| \ll \sqrt{N_q}\, u.
\tag{10}
$$

4.2 Resonance with betatron frequency

Then the expectation value of the vibration of the beam at the IP, $\langle |\Delta y^*|^2 \rangle$ is obtained by averaging Eq. (5) over ϕ_q as:

$$
\begin{aligned}
\langle |\Delta y^*|^2 \rangle &= \frac{1}{2\pi} \int |\Delta y^*|^2 \, d\phi_q \\
&= \frac{\beta^* \beta_q k_q^2 \langle \Delta y_q^2 \rangle}{4} \frac{\exp(\alpha)(\cosh\alpha - \cos\mu_q \cos\mu_y)}{(\cosh\alpha - \cos(\mu_q - \mu_y))(\cosh\alpha - \cos(\mu_q + \mu_y))}.
\end{aligned}
\tag{11}
$$

Thus the vibration at the IP has resonances at $\mu_q = \pm\mu_y + 2m\pi$ with an integer m.

Figure 13 A ground vibration measurement performed at CERN site by M. Serluca, et al. [25]. The dashed line is a rough fit of the spectrum by these authors

By assuming the spectrum of $\langle \Delta y_q^2 \rangle$ is uniform around each resonance, the vibration at the IP can be evaluated as:

$$\langle |\Delta y^*|^2 \rangle = \frac{\beta^* \beta_q k_q^2}{8\alpha T_0} \sum_m S\big((\pm\mu_y \pm 2m\pi)/T_0\big), \tag{12}$$

where $S(\omega)$ is the power spectrum density of $\langle \Delta y_q^2(\omega) \rangle$, and we have assumed $\cos\mu_q \cos\mu_y \sim 1/2$ and $\alpha \ll 1$.

A measurement of ground vibration done at CERN tells us

$$S(\omega) = \sigma\omega^{-4} \sim 10^{-15} \left(\frac{\omega}{2\pi\,\mathrm{Hz}}\right)^{-4} \mathrm{m^2/Hz}, \tag{13}$$

with a coefficient σ as shown in Fig. 13. Then among the resonances only the lowest one $m \sim \mu_y/2\pi$ will matter. In the case of FCC-ee, this lowest resonance appears at the resonant frequency

$$\omega/2\pi = \omega_r/2\pi \sim (1.2, 1.8)\ \mathrm{kHz}, \tag{14}$$

corresponding to $[\mu_y/2\pi] \sim (0.4, 0.6)$, resulting in

$$S(\omega_r) \sim (4.8, 0.95) \times 10^{-28}\ \mathrm{m^2/Hz}. \tag{15}$$

Plugging in the following FCC-ee Z lattice parameter value:

$$\begin{aligned}
&\beta^* = 0.8\ \mathrm{mm}, &&\langle\beta\rangle = 436\ \mathrm{m}, \\
&\langle k_q^2 \rangle^{1/2} = 0.045\ /\mathrm{m}, &&\langle\beta k_q^2\rangle = 8.5\ /\mathrm{m}, \\
&\alpha = 4.3 \times 10^{-4}, &&T_0 = 304\ \mu s
\end{aligned} \tag{16}$$

into Eq. ([12]) and multiplying by the number of all quadrupoles N_q = 1856, we get

$$\sqrt{\Delta y^{*2}} \sim 13.7\text{pm,} \tag{17}$$

which is considerably smaller than the IP vertical beam size of $\sim$ 37 nm.

4.3 Non-resonant vibration

Next let us look at the off-resonant contribution of Eq. ([11]), If we roughly approximate the tune-dependent term by 1, the integrated power spectrum in a range $\omega \geq \omega_c$ is given as

$$\begin{aligned}
\sqrt{\Delta y^{*2}} &= \frac{N_q \beta^* \beta_q k_q^2}{4} \int_{\omega_c}^{\infty} S(\omega) \frac{d\omega}{2\pi} \\
&= \frac{N_q \beta^* \beta_q k_q^2 \sigma}{24\pi \omega_c^3}.
\end{aligned} \tag{18}$$

In the case for the previous measurement, we estimate $\sigma \sim 1.6 \times 10^{-12}$ m^2/Hz, then

$$\sqrt{\Delta y^{*2}} \sim 32.3 \text{ nm} \tag{19}$$

for $\omega_c = 2\pi \times 1$Hz. The assumption here is that below the critical frequency ω_c, an orbit feedback suppresses the beam oscillation perfectly. Thus the expected vibration reaches to the vertical beam size at the IP.

Among the vibration, the dominant contribution is from the defocusing final quadrupoles around the IP (named "QC[12]*") which reaches

$$\sqrt{\Delta y^{*2}}_{\text{QC[12]}*} \sim 31.9 \text{ nm.} \tag{20}$$

Thus suppressing the vibration of the final quadrupoles and a feedback system working beyond 1 Hz hopefully up to 10 Hz will be crucial. We note again that no amplification of the vibration due to the supporting structure is taken into account.

However, up to frequencies of about 100 Hz ($\sim$3% of the revolution frequency), what mostly matters is the relative vertical quadrupole vibration for the two beams. Without such a relative motion the vertical closed orbits of electrons and positrons follow each other as long as the vibration frequencies are small compared with the revolution frequency. Since the final quadrupole is conceived as a "twin" magnet, with superconducting windings inside a common cryostat [1], it should be possible—in the frequency range of interest—to damp or suppress this harmful asymmetric vibration mode, where the magnetic field center moves vertically upwards for the electron beam while it descends for the adjacent positrons.

5 Conclusions

The optical lattice of the large $\sim$ 100 km FCC-ee collider presents unique challenges. Reaching a target luminosity above 10^{34} cm^{-2}s^{-1} in each of up to four collision points at the $t\bar{t}$ energy (182.5 GeV/beam) sets stringent requirements both for the arc optics and for the optics around the interaction points, with β_y^* values of order 1 mm. Along with establishing the IP optics parameters, an adequate correction of the arc optics and control of the beam emittance are must, for all four operation modes of the collider.

Emittance tuning of such a large storage ring, therefore, is a condition sine qua non for successful operation, and the associated tolerances on magnet fields and position alignments have to be carefully determined. The large ring size, large natural chromaticity, small β_y^*, the targeted low vertical emittance and the small coupling ratio renders the FCC-ee design sensitive to misalignments and field errors.

For the arcs, the assumed dipole rms alignment errors of 1 mm are extremely relaxed. The rms arc girder alignments of 150 μm and quadrupole/sextupole magnet alignment tolerances of 50 μm rms with respect to the girder, also appear within reach of conventional alignment methods. These tolerances are less strict than those contemplated for many next generation storage-ring light sources, though the large size of the FCC-ee ring and longer cell length may conceivably introduce new challenges. The field error tolerances are also similar to what is already achieved at many light source facilities.

In the analytical investigations and simulation presented here, we studied the impact of the assumed magnet alignments. The correction algorithms developed in this context represent a powerful correction tools and lead to successful convergence for the majority of the applied errors seeds, with a median vertical emittance 0.90 pm and a horizontal emittance of 1.50 nm. Whilst the emittance tuning studies are on-going, the preliminary results presented provide a promising indication that realistic misalignment and field error tolerances, along with further developed correction methods, can lead to the desired low levels of coupling and beam emittance. Further work is need to investigate non-linear terms that reduce the dynamic aperture.

The colliding beams at the FCC-ee can be vertically offset due to magnet vibrations. Most critical is the relative vertical motion of the final electron and positron quadrupoles, which are located inside a common cryostat. This relative vibration must be controlled and minimised.

Declarations

Competing interests
The authors declare that they have no competing interests.

Author contributions
All authors read and approved the final manuscript.

Author details
[1]Department of Physics, University of Liverpool, Liverpool, UK. [2]Cockcroft Institute, Warrington, UK. [3]Beams Department, CERN, Geneva, Switzerland. [4]KEK, Oho, Tsukuba, Ibaraki, Japan. [5]École Polytechnique Fédérale de Lausanne (EPFL), Lausanne, Switzerland.

Publisher's Note

Springer Nature remains neutral with regard to jurisdictional claims in published maps and institutional affiliations.

References

1. Benedikt M et al. Future circular collider study the lepton collider (FCC-ee). Eur Phys J C. 2019;79:474.
2. Kubo K. Simulation study of low emittance tuning of the accelerator test facility damping ring at KEK. Phys Rev Spec Top, Accel Beams. 2003;6(9):39–49. https://doi.org/10.1103/PhysRevSTAB.6.092801.
3. Hellert T, Amstutz P, Steier C, Venturini M. Toolkit for simulated commissioning of storage-ring light sources and application to the advanced light source upgrade accumulator. Phys Rev Accel Beams. 2019;22(10):100702. https://doi.org/10.1103/PhysRevAccelBeams.22.100702.
4. Sajaev V. Commissioning simulations for the argonne advanced photon source upgrade lattice. Phys Rev Accel Beams. 2019;22(4):40102. https://doi.org/10.1103/PhysRevAccelBeams.22.040102.
5. Dalena B, Barranco J, Latina A, Marin E, Pfingstner E, Schulte D, Snuverink J, Tomas R, Zamudio G. Beam delivery system tuning and luminosity monitoring in the compact linear collider. Phys Rev Accel Beams. 2012;15:05006. https://doi.org/10.1103/PhysRevSTAB.15.051006.
6. Ögren J, Latina A, Schulte D, Tomas R. Tuning the compact linear collider 380 gev final-focus system using realistic beam-beam signals. Phys Rev Accel Beams. 2020;23:05102. https://doi.org/10.1103/PhysRevAccelBeams.23.051002.
7. Carlier FS, et al. Optics Measurements and Correction Challenges for the HL-LHC. 2017. https://doi.org/10.5170/CERN-ACC-2017-0088.
8. Thrane P, Tomas R, Koval A, Ohmi K, Ohnishi Y, Wegscheider A. Measuring β^* in superkekb with k modulation. Phys Rev Accel Beams. 2019;23:012803. https://doi.org/10.1103/PhysRevAccelBeams.23.012803.
9. Koratzinos M. Update on IR compensation scheme. 118th FCC-ee Optics Design Meeting, 8 May 2020. https://indico.cern.ch/event/915196/.
10. Oide K, El Khechen D. Beam blowup due to synchro-beta resonance with/without beam-beam effects. In: eeFACT 2018—proceedings of the 62nd ICFA advanced beam dynamics workshop on high luminosity circular e^+e^- colliders. 2019. p. 207–11. https://doi.org/10.18429/JACoW-eeFACT2018-WEXBA03.
11. El Khechen D, Oide K, Zimmermann F. Beam-beam blowup in the presence of X-Y coupling sources at FCC-ee. In: eeFACT 2018—proceedings of the 62nd ICFA advanced beam dynamics workshop on high luminosity circular e^+e^- colliders. 2019. p. 112–5. https://doi.org/10.18429/JACoW-eeFACT2018-TUYBA03.
12. FCC-ee-lattice gitlab repository (2021). https://gitlab.cern.ch/fcc-optics/FCC-ee-lattice
13. Deniau L. Methodical Accelerator Design. MAD-X User's Reference Manual. http://madx.web.cern.ch.
14. Raubenheimer TO. Tolerances to limit the vertical emittance in future storage rings. Part Accel. 1991;36:75–119. https://doi.org/10.1080/1071441950170102.
15. Wolski A. Low-emittance storage rings. In: CERN accelerator school CAS 2013: advanced accelerator physics course. Trondheim, Norway. 18–29 August 2013. 2015. p. 245–94. https://doi.org/10.5170/CERN-2014-009.245.
16. Panagiotidis K, Wolski A. Alignment sensitivities in the ILC damping rings. In: Proceedings of the IEEE particle accelerator conference. 2007. p. 2877–9. https://doi.org/10.1109/PAC.2007.4440606.
17. Charles TK, Aumon S, Holzer B, Oide K, Zimmermann F. Low emittance tuning of FCC-ee. J Phys Conf Ser. 2019;1350(1):012006. https://doi.org/10.1088/1742-6596/1350/1/012006.
18. Charles TK, Holzer B, Oide K, Zimmermann F. Update on the low emittance tuning of the e^+e^- future circular collider. In: Proc. 12th int. particle acc. conf. (IPAC21) (WEPAB011). 2021. p. 2601–4. https://doi.org/10.18429/JACoW-IPAC2021-WEPAB011.
19. Härer B, Doblhammer A, Holzer BJ. Tapering Options and Emittance Fine Tuning for the FCC-ee Collider. In: Proc. Of international particle accelerator conference (IPAC'16). International Particle Accelerator Conference. Busan, Korea. May 8–13, 2016. Geneva, Switzerland: JACoW; 2016. p. 3767–70. https://doi.org/10.18429/JACoW-IPAC2016-THPOR003.
20. Chao AW. Evaluation of beam distribution parameters in an electron storage ring. J Appl Phys. 1979;50(595):2143.
21. Oide K, Aiba M, Aumon S, Benedikt M, Blondel A, Bogomyagkov A, Boscolo M, Burkhardt H, Cai Y, Doblhammer A, Haerer B, Holzer B, Jowett JM, Koop I, Koratzinos M, Levichev E, Medina L, Ohmi K, Papaphilippou Y, Piminov P, Shatilov D, Sinyatkin S, Sullivan M, Wenninger J, Wienands U, Zhou D, Zimmermann F. Design of beam optics for the future circular collider e^+e^- collider rings. Phys Rev Accel Beams. 2016;19:111005. https://doi.org/10.1103/PhysRevAccelBeams.19.111005.
22. Baklakhov A. Sov Phys J. 1993;TF63 10.
23. Wolski A, Walker NJ. A model OF ATL ground motion for storage rings. In: Proc. of the 2003 particle accelerator conference. 2003. p. 2396.
24. Rossbach J. Closed orbit distortions of periodic fodo lattices due to plane ground waves. Part Accel. 1988;50(23):121.
25. Serluca M et al. Vibration Analysis and Control in Particle Accelerator. Workshop on the mechanical optimisation of the FCC-ee (2018). https://indico.cern.ch/event/694811/contributions/2863859/attachments/1595533/2526938/2018_02_06_FCCee_MDI_workshop_Serluca.pdf